Published in IET Microwaves, Antennas & Propagation
Received on 5th October 2012
Revised on 10th April 2013
Accepted on 24th May 2013
doi: 10.1049/iet-map.2013.0090

ISSN 1751-8725

$\mathcal{H}^2$-matrix-based fast volume integral equation solver for electrodynamic analysis

Saad Omar, Dan Jiao

School of Electrical and Computer Engineering, Purdue University West Lafayette, IN 47907, USA
E-mail: djiao@purdue.edu

Abstract: An $\mathcal{H}^2$-matrix-based mathematical framework is introduced and further developed to reduce the computational complexity of the volume integral equation (VIE)-based analysis of electrodynamic problems. Numerical experiments have demonstrated a significant reduction in CPU time and memory consumption. A linear scaling with respect to matrix size in both CPU time and memory is achieved for small and medium-sized electrodynamic problems with an interpolation-based $\mathcal{H}^2$-representation of the VIE operator in conjunction with a rank function for accuracy control. The proposed solver is applicable to arbitrarily shaped three-dimensional structures immersed in inhomogeneous materials.

1 Introduction

The ever-expanding world of electromagnetic analysis is setting new challenges for computational electromagnetics scientists everyday. Not only are electromagnetic analysis and design methods pivotal in advanced engineering systems but also find enormous applications in the fields of medicine and defence. In particular, the interaction of electromagnetic waves with dielectric bodies is central in highly complicated areas like radio-wave propagation, scattering by and detection of airborne particulates, radome design, non-linear eddy current analysis, surface tomography, analysis of scattering by anisotropic and highly contrast complex media like magnetic photonic crystals and medical diagnostics. However, the demands of these highly complex areas and the continued increase in the complexity of engineering systems are yet to be met at the same rate. To synchronise the pace of developing electromagnetic methods with that of its demands, it is of critical importance to develop computational electromagnetic methods the complexity of which scales favourably with the problem size.

Methods in computational electromagnetic can be classified into two classes: integral equation (IE)-based methods and partial differential equation-based ones. IE-based methods generally lead to dense systems of linear equations. When a conventional direct method is used, the memory requirements are $O(N^2)$, whereas the operation counts are proportional to $O(N^3)$, where N is the dimension of the matrix. The utilisation of iterative methods only helps in reducing time complexity to $O(N_{\text{it}}N^2)$, where N_{it} is the iteration number to attain convergence. In recent decades, fast solvers [1–6] such as fast multipole methods and fast Fourier transform-based methods have dramatically reduced the storage requirements and time complexity of iterative solvers to $O(N\log N)$ in each iteration for electrodynamic analysis. These represent an impressive improvement over the conventional $O(N^3)$ or $O(N^2)$ techniques.

Recently, in [7, 8], an $\mathcal{H}^2$-matrix-based mathematical framework was introduced and further developed to reduce the computational complexity of a surface integral equation-based analysis of electrodynamic problems. In an $\mathcal{H}^2$-matrix [9, 10], all off-diagonal blocks which describe the interaction between two separated geometry blocks are represented by a factorised low rank form which has a nested property. Besides a hierarchical low-rank representation, the $\mathcal{H}^2$-framework also encompasses a system of fast arithmetics which permits compact storage and efficient computation of dense matrices. There has been a question on whether an error-bounded low-rank approximation of integral operators exists for electrodynamic analysis regardless of electric size. This question has been answered by a theoretical study of the rank of the integral operators [11, 12]. This study proves that the minimal rank of the interaction between two separated geometry blocks in an integral-equation-based analysis of general three-dimensional (3D) objects, for a prescribed error bound, scales linearly with the electric size of the block diameter. Since the number of unknowns in a surface IE-based analysis scales as electric size square, and that in a volume IE-based analysis scales as electric size cube, the existence of the error-bounded low-rank representation of both surface and volume integral operators is proved for electrodynamic analysis, irrespective of electric size. Methods which do not generate a minimal rank approximation for a prescribed accuracy can result in a rank that scales with electric size at a much higher rate. However, they do not reflect the actual rank required for satisfying the prescribed accuracy. In [7], a rank function

is proposed to control the growth of the rank with electric size to maintain a desired order of accuracy in a fairly wide range of electric sizes from small to medium electric sizes, without compromising the computational complexity. Using this rank function and the $\mathcal{H}^2$-matrix as a mathematical framework, in [7, 8] it is demonstrated that from small to tens of wavelengths, the dense system of $O(N^2)$ non-zero entries can be compactly stored in $O(N)$ memory units, thereby allowing for a dense matrix–vector multiplication to be accomplished in $O(N)$ CPU operations.

The major contribution of this work is that we achieved a similar reduction in computational cost for a volume integral equation (VIE)-based analysis of small and medium-sized electrodynamic problems. It is well known that the solution to inhomogeneous problems are better addressed by VIE solvers than surface IE solvers. Compared with a dense system formulated from a surface IE-based analysis, the dense system constructed from a volume IE-based analysis is much more complicated. The VIE-based system consists of all four possible forms of double integrals characterising volume–volume, volume–surface, surface–volume and surface–surface interactions, respectively, resulting in a much larger and much more complex linear system of equations. The underlying numerical system is also truly 3D as compared with that of a surface IE in which a 2D based interpolation can be applied. In this paper, we are able to overcome the numerical challenge associated with a VIE-based analysis and successfully develop an $\mathcal{H}^2$-based VIE solution. This solution significantly reduces the computational cost of solving a VIE-based dense system for electrodynamic analysis. Numerical experiments from small electric sizes to 32 wavelengths have demonstrated a clear linear scaling of the proposed method in both CPU time and memory consumption, with prescribed accuracy achieved in the electric size range. Application to electrically even larger problems such as a dielectric rod of 80 wavelengths, also, demonstrates the accuracy and efficiency of the proposed solver. Multiple numerical examples, including both homogeneous and inhomogeneous cases, validate the accuracy and computational advantages of the proposed $\mathcal{H}^2$-based VIE solution.

The remainder of this paper is organised as follows. In Section 2, we formulate the volume integral equation. In Section 3, we propose an $\mathcal{H}^2$-matrix-based representation of the VIE dense system of equations. In Section 4, we present a fast $\mathcal{H}^2$-based VIE solver which has compact storage and efficient matrix–vector multiplication. Section 5 contains the numerical results which demonstrate the accuracy and efficiency of the proposed solver as compared with its conventional counterpart. The concluding remarks are drawn in Section 6.

2 VIE formulation

Consider an arbitrarily shaped 3D inhomogeneous dielectric body of complex permittivity $\varepsilon(r)$ occupying volume V, which is exposed to an incident field $\boldsymbol{E}^{\mathrm{i}}(\boldsymbol{r})$. The scattered field because of the equivalent volume polarisation current $\boldsymbol{J}$ contributes to the total field at any point $\boldsymbol{r}$ in the sense as expressed in the form of the following volume integral equation

$$E^i(\boldsymbol{r}) = \frac{D(\boldsymbol{r})}{\epsilon(r)} - \int_V \mu_0\omega^2\kappa(\boldsymbol{r}')D(\boldsymbol{r}')g(\boldsymbol{r},\ \boldsymbol{r}')\ \mathrm{d}v' - \int_V \nabla\left[\nabla'\left(\kappa(\boldsymbol{r})\frac{D(\boldsymbol{r}')}{\epsilon_0}\right)\right]g(\boldsymbol{r},\ \boldsymbol{r}')\ \mathrm{d}v' \tag{1}$$

where $g(\boldsymbol{r},\ \boldsymbol{r}') = \mathrm{e}^{-\mathrm{j}k_0|\boldsymbol{r}-\boldsymbol{r}'|}/4\pi|\boldsymbol{r}-\boldsymbol{r}'|$, ω being the angular frequency, κ is the contrast ratio defined as $(\varepsilon(\boldsymbol{r})-\varepsilon_0)/\varepsilon(\boldsymbol{r})$, $\boldsymbol{D}(\boldsymbol{r}')$ is the electric flux density, whereas k_0 is the free space wavenumber. By expanding the unknown electric flux density $\boldsymbol{D}(\boldsymbol{r}')$ in terms of SWG basis functions $\boldsymbol{D}_n(\boldsymbol{r}')$ each with a coefficient D_n, and then testing the resulting equation using Galerkin method with $\boldsymbol{D}_m(\boldsymbol{r})$, we obtain the following linear system of VIE (see equation at the bottom of the page)

which can be written as a matrix equation

$$\boldsymbol{SD} = \boldsymbol{E} \tag{2}$$

where

$$E_m = \int_{V_m} \boldsymbol{E}^i \cdot \boldsymbol{D}_m(\boldsymbol{r})\ \mathrm{d}v$$

$$S = \boldsymbol{\Lambda} + \boldsymbol{G}; \quad \boldsymbol{\Lambda}_{mn} = \int_{V_m} \frac{\boldsymbol{D}_m(\boldsymbol{r})}{\epsilon(\boldsymbol{r})} \cdot \boldsymbol{D}_n(\boldsymbol{r})\ \mathrm{d}v$$

$$\begin{aligned}\int_{V_m} \boldsymbol{E}^i(\boldsymbol{r}) \cdot \boldsymbol{D}_m(\boldsymbol{r})\,\mathrm{d}v = \sum_{n=1}^{N} \boldsymbol{D}_n \Bigg[& \int_{V_m} \frac{\boldsymbol{D}_m(\boldsymbol{r})}{\epsilon(\boldsymbol{r})} \cdot \boldsymbol{D}_n(\boldsymbol{r})\ \mathrm{d}v \\ & - \mu_0\omega^2 \int_{V_m} \boldsymbol{r} \int_{V_n} \kappa(\boldsymbol{r}')\boldsymbol{D}_m(\boldsymbol{r}) \cdot \boldsymbol{D}_n(\boldsymbol{r}')g(\boldsymbol{r},\boldsymbol{r}')\mathrm{d}v'\mathrm{d}v \\ & - \frac{1}{\epsilon_0}\Bigg(\int_{S_m} \int_{V_n} \kappa(\boldsymbol{r}')\big(\boldsymbol{D}_m(\boldsymbol{r}) \cdot \hat{n}\big)\big(\nabla' \cdot \boldsymbol{D}_n(\boldsymbol{r}')\big)g(\boldsymbol{r},\boldsymbol{r}')\mathrm{d}v'\mathrm{d}s \\ & + \int_{S_m} \int_{S_n} \big(\kappa^+(\boldsymbol{r}') - \kappa^-(\boldsymbol{r}')\big)\big(\boldsymbol{D}_m(\boldsymbol{r}) \cdot \hat{n}\big)\big(\boldsymbol{D}_n(\boldsymbol{r}') \cdot \hat{n}'\big)g(\boldsymbol{r},\boldsymbol{r}')\mathrm{d}s'\mathrm{d}s \\ & - \int_{V_m} \int_{V_n} \kappa(\boldsymbol{r}')\big(\nabla \cdot \boldsymbol{D}_m(\boldsymbol{r})\big)\big(\nabla' \cdot \boldsymbol{D}_n(\boldsymbol{r}')\big)g(\boldsymbol{r},\boldsymbol{r}')\mathrm{d}v'\mathrm{d}v \\ & - \int_{V_m} \int_{S_n} \big(\kappa^+(\boldsymbol{r}') - \kappa^-(\boldsymbol{r}')\big)\big(\nabla \cdot \boldsymbol{D}_m(\boldsymbol{r})\big)\big(\boldsymbol{D}_n(\boldsymbol{r}') \cdot \hat{n}'\big)g(\boldsymbol{r},\boldsymbol{r}')\mathrm{d}s'\mathrm{d}v \Bigg)\Bigg]\end{aligned}$$

doi: 10.1049/iet-map.2013.0090

(see equation at the bottom of the page)

A straightforward approach to solve the above complex dense system of equations can be as expensive as $O(N^2)$. Our approach is centred on finding an error-controlled $\mathcal{H}^2$-representation of $\boldsymbol{G}$, which will be referred to as $\boldsymbol{G}_i$s $(1 \le i \le 4)$ corresponding to the volume–volume, volume–surface, surface–volume and surface–surface interaction, respectively, shown in $\boldsymbol{G}_{mn}$ above. Thus, $\boldsymbol{G}$ as a whole can be specified by a reduced set of parameters, whereas $\boldsymbol{\Lambda}$ is intrinsically sparse. Hence, an overall reduction in memory and operation counts can be achieved.

3 Proposed $\mathcal{H}^2$-based representation of VIE system

In the proposed VIE solver, the very first step is to approximate each of the dense matrix terms $\boldsymbol{G}_i$ by a corresponding $\mathcal{H}^2$-matrix with error well controlled, whose details are elaborated in Section 3.1. Then, in Section 3.2, we discuss how we exploit the block cluster tree to capture the nested hierarchical dependencies present in an $\mathcal{H}^2$-matrix representation for compact storage and efficient computation. In Section 3.3, we present a rank function and analyse how to control the accuracy of an interpolation-based $\mathcal{H}^2$-representation of the VIE operator via the rank function.

3.1 $\mathcal{H}^2$-Representation and its error bound

A close observation of the four different types of terms in $\boldsymbol{G}$ of (2) reveals that each of these four terms (represented throughout the paper as $\boldsymbol{G}_i$) can be written as

$$\boldsymbol{G}_i = K \int_{P_m} f_m(\boldsymbol{r}) \int_{Q'_n} g(\boldsymbol{r},\ \boldsymbol{r}') f_n(\boldsymbol{r}')\ \mathrm{d}q'\ \mathrm{d}p \tag{3}$$

where K is a constant which is different in each $\boldsymbol{G}_i$, $f_m(\boldsymbol{r})$ and $f_n(\boldsymbol{r}')$ can be any of the scalar terms or the basis functions, depending on the types of $\boldsymbol{G}_i$ they are a part of, whereas $P_m(Q'_n)$ can be any one of $V_m(V_n)$ or $S_m(S_n)$, thus generalising each of the terms in $\boldsymbol{G}$.

There are multiple ways of generating an $\mathcal{H}^2$-representation of the dense matrix $\boldsymbol{G}_i$. Here, we employ an interpolation-based method with a rank function to construct an $\mathcal{H}^2$-representation of $\boldsymbol{G}_i$. This method does not incur any compression cost for generating the $\mathcal{H}^2$-representation. Meanwhile, its accuracy can be controlled to a desired order without sacrificing computational efficiency in a fairly wide range of electric sizes from small to medium sizes by the use of a rank function, which will be elaborated in Section 3.3.

The details of the interpolation-based $\mathcal{H}^2$-representation of a VIE dense system are as follows. We fix two subsets t and s of the full index set of basis functions $\mathcal{I} := \{1,\ 2,\ \ldots,\ N_{\psi,\mathcal{I}}\}$ and $\mathcal{J} := \{1,\ 2,\ \ldots,\ N_{\phi,\mathcal{J}}\}$ used in the discretisation of $\boldsymbol{G}_i$. Here, $N_{\psi(\phi),\mathcal{I}(\mathcal{J})}$ may represent the number of $\boldsymbol{D}_{m(n)}$ in a continuous volume, the number of $\boldsymbol{D}_{m(n)}$ at a discontinuity or the number of $\boldsymbol{D}_{m(n)}$ on the outermost boundary, which need not be the same in both $\mathcal{I}$ and $\mathcal{J}$. The corresponding domains Ω_t and Ω_s are defined to be the union of the supports of the basis functions, that is

$$\Omega_t := \bigcup_{i \in t} \mathrm{supp}(\boldsymbol{D}_i), \quad \Omega_s := \bigcup_{i \in s} \mathrm{supp}(\boldsymbol{D}_i) \tag{4}$$

If diam(.) and dist(.,.), respectively, denote the Euclidean diameter of a set and Euclidean distance between any two sets and

$$\max\{\mathrm{diam}\ (\Omega_t),\ \mathrm{diam}\ (\Omega_s)\} \le \eta\ \mathrm{dist}\ (\Omega_t,\ \Omega_s) \tag{5}$$

in which η is a positive parameter, t and s are said to be admissible [10]. The original kernel function $g(\boldsymbol{r}, \boldsymbol{r}')$ in (3) for admissible $(t,\ s)$ can be replaced by a degenerate approximation

$$\tilde{g}^{t,\,s} = \sum_{\nu \in K^t} \sum_{\mu \in K^s} g\left(\xi^t_\nu,\ \xi^s_\mu\right) L^t_\nu(\boldsymbol{r}) L^s_\mu(\boldsymbol{r}') \tag{6}$$

where $K := \{\nu \in \mathbb{N}^3 : \nu_i \le p,\ \forall i \in \{1,\ \ldots,\ 3\}\} = \{1,\ \ldots,\ p\}^3$; p is the number of interpolation points along each dimension; $\left(\xi^t_\nu\right)_{\nu \in K^t}$ is a family of interpolation points in t; $\left(\xi^s_\mu\right)_{\mu \in K^s}$ is a family of interpolation points in s; and $\left(L^t_\nu\right)_{\nu \in K^t}$ and $\left(L^s_\mu\right)_{\mu \in K^s}$ are the corresponding Lagrange polynomials. The degenerate approximation of (6) allows for separation of the double integral in (3) into

$$\tilde{\boldsymbol{G}}_i = K \sum_{\nu \in K^t} \sum_{\mu \in K^s} g\left(\xi^t_\nu,\ \xi^s_\mu\right) \times \int_{P_m} f_m(\boldsymbol{r}) L^t_\nu(\boldsymbol{r})\ \mathrm{d}p \int_{Q'_n} f_n(\boldsymbol{r}') L^s_\mu(\boldsymbol{r}')\ \mathrm{d}q' \tag{7}$$

$$\begin{aligned} G_{mn} = {} & -\mu_0 \omega^2 \int_{V_m} \int_{V_n} \kappa(\boldsymbol{r}') \boldsymbol{D}_m(\boldsymbol{r}) \cdot \boldsymbol{D}_n(\boldsymbol{r}) g(\boldsymbol{r},\ \boldsymbol{r}')\ \mathrm{d}v'\ \mathrm{d}v \\ & - \frac{1}{\epsilon_0} \left(\int_{S_m} \int_{V_n} \kappa(\boldsymbol{r}') \left(\boldsymbol{D}_m(\boldsymbol{r}) \cdot \hat{n}\right) \left(\nabla' \cdot \boldsymbol{D}_n(\boldsymbol{r}')\right) g(\boldsymbol{r},\ \boldsymbol{r}')\ \mathrm{d}v'\ \mathrm{d}s \right. \\ & + \int_{S_m} \int_{S_n} \left(\kappa^+(\boldsymbol{r}') - \kappa^-(\boldsymbol{r}')\right) \left(\boldsymbol{D}_m(\boldsymbol{r}) \cdot \hat{n}\right) \left(\boldsymbol{D}_n(\boldsymbol{r}') \cdot \hat{n}'\right) g(\boldsymbol{r},\ \boldsymbol{r}')\ \mathrm{d}s'\ \mathrm{d}s \\ & - \int_{V_m} \int_{V_n} \kappa(\boldsymbol{r}') \left(\nabla \cdot \boldsymbol{D}_m(\boldsymbol{r})\right) \left(\nabla' \cdot \boldsymbol{D}_n(\boldsymbol{r}')\right) g(\boldsymbol{r},\ \boldsymbol{r}')\ \mathrm{d}v'\ \mathrm{d}v \\ & \left. - \int_{V_m} \int_{S_n} \left(\kappa^+(\boldsymbol{r}') - \kappa^-(\boldsymbol{r}')\right) \left(\nabla \cdot \boldsymbol{D}_m(\boldsymbol{r})\right) \left(\boldsymbol{D}_n(\boldsymbol{r}') \cdot \hat{n}'\right) g(\boldsymbol{r},\ \boldsymbol{r}')\ \mathrm{d}s'\ \mathrm{d}v \right) \end{aligned}$$

thereby yielding the following factorisation of $\tilde{\boldsymbol{G}}_i$

$$\tilde{\boldsymbol{G}}_i = \boldsymbol{V}^t \boldsymbol{S}^{t,s} \boldsymbol{V}^{sT}; \quad \boldsymbol{V}^t \in \mathbb{R}^{t \times K^t}, \quad \boldsymbol{S}^{t,s} \in \mathbb{C}^{K^t \times K^s}, \quad \boldsymbol{V}^s \in \mathbb{R}^{s \times K^s} \tag{8}$$

where

$$V^t_{m,\nu} = \int_{P_m} f_m(\boldsymbol{r}) L^t_\nu(\boldsymbol{r})\, \mathrm{d}p, \quad m \in t,\ \nu \in K^t$$
$$V^s_{n,\mu} = \int_{Q'_n} f_n(\boldsymbol{r}') L^s_\mu(\boldsymbol{r}')\, \mathrm{d}q', \quad n \in s,\ \mu \in K^s \tag{9}$$
$$\boldsymbol{S}^{t,s}_{\nu,\mu} = Kg\left(\xi^t_\nu,\ \xi^s_\mu\right), \quad \nu \in K^t,\ \mu \in K^s$$

In comparison with (7), $\boldsymbol{V}^t(\boldsymbol{V}^s)$ represent the integral over the $P_m(Q_{n'})$ domain whereas $\boldsymbol{S}^{t,s}$ represents the constant K multiplied by $g\left(\xi^t_\nu,\ \xi^s_\mu\right)$. Clearly, the rank of each $\tilde{\boldsymbol{G}}_i$ is independent of the cardinality of either s or t and is at most the cardinality of $K^t(K^s)$ if the latter is less than the former. As can be seen from (7), the cardinality of K^t or K^s is p^3 in a VIE system. The p in this work is controlled by a rank function to be discussed in Section 3.3. Now, $\tilde{\boldsymbol{G}}_i$ in (8) constitutes an $\mathcal{H}^2$-representation of $\boldsymbol{G}_i$ in (3) provided the same space of polynomials are used across t and s.

As shown in [7], once the admissibility criterion of (5) is satisfied, the maximum approximation error of (6) is bounded by (see (10))
where α_p is a constant related to interpolation, k_0 is the wavenumber and $d = 3$ for a VIE.

In (10), the last term has an exponential decay rate with respect to p. It is clear that exponential convergence with respect to p can be obtained irrespective of the electric size ($k_0\eta$ dist(Ω_t, Ω_s)) [It can be seen from (5) that $k_0\eta$ dist(Ω_t, Ω_s) is proportional to the electric size of the largest block diameter of Ω_t and Ω_s]. In addition, given a required level of accuracy, when the electric size increases, the error of the approximation can be controlled to the required level by increasing the number of interpolation points p. With the controlled error explained, we now can analyse the difference between p chosen for small electric sizes and that for large electric sizes. It can be seen from (10) that p required for large electric sizes is larger than that for small electric sizes to achieve the same accuracy. For very large electric sizes, to obtain a good accuracy of (10), asymptotically, p has to be chosen proportional to the electric size of the block diameter. This renders the interpolation based $\mathcal{H}^2$-representation not efficient for computing electrically large problems although good accuracy can still be obtained by choosing a large p. However, this does not mean that $\mathcal{H}^2$-based methods do not apply to electrically large problems. The $\mathcal{H}^2$-based methods encompass both $\mathcal{H}^2$-based representations of a dense matrix and the $\mathcal{H}^2$-based fast matrix computation. In addition to the interpolation-based $\mathcal{H}^2$-representation which does not generate a minimal rank representation of the integral operator because it separates sources from observers in approximating Green's function [11, 12], there exist other minimal-rank-based $\mathcal{H}^2$-representations which are efficient for computing electrically large problems [12, 13].

3.2 Cluster tree and block cluster tree construction

Once the admissibility criterion is set, the next step is to partition the product index set $\mathcal{I} \times \mathcal{J}$ into admissible and inadmissible blocks to realise efficient computation using the cluster tree and block cluster tree [9, 10].

The 3D computational domain which comprises the SWG basis functions is recursively split into subdomains till the number of unknowns in each subdomain becomes less or equal to the 'leafsize' ($n_{\min}$), hence, essentially $n_{\min}$ controls the depth of the tree. Each set of bases lying in a subdomain are said to form a 'cluster', we can thus say that a 'cluster tree' $T_{\mathcal{I}}$ is generated. Clusters with indices less than or equal to $n_{\min}$ are 'leaves' denoted by $\mathcal{L}_{\mathcal{I}}$. Now, the construction of any admissible 'block cluster tree' from the cluster trees $T_{\mathcal{I}}$ and $T_{\mathcal{J}}$ (in accordance with the admissibility condition) is achieved recursively as follows.

As already mentioned, $\mathcal{I}$ is not necessarily the same as $\mathcal{J}$ in a VIE-based formulation. Visualising $T_{\mathcal{I}}$ to be placed in parallel with $T_{\mathcal{J}}$, we check blocks level by level starting with Root($T_{\mathcal{I}}$) and Root($T_{\mathcal{J}}$), and then descending the tree. For instance, given two clusters $t \in T_{\mathcal{I}}$ and $s \in T_{\mathcal{J}}$, we check the admissibility condition, if it is not satisfied, we repeat the procedure for all the combinations of children(t) and children(s). This results in an admissible block cluster tree defining a matrix structure and each 'leaf block cluster', $\mathcal{L}_{\mathcal{I}\times\mathcal{J}}$. The admissible blocks denoted in [7] by $\mathcal{L}^+_{\mathcal{I}\times\mathcal{J}}$ and the inadmissible blocks denoted by $\mathcal{L}^-_{\mathcal{I}\times\mathcal{J}}$ have an $\mathcal{H}^2$-matrix-based low-rank approximation and a full matrix representation, respectively. Owing to the appearance of all the four possible combinations of integrals in a VIE system matrix, four block cluster trees are constructed. Of these four, two that represent the interactions via volume–volume integration and (boundary)surface–(discontinuous)surface integration are constructed based on the same pattern as in [7]. The other two cluster trees are novel in the sense that they result in unsymmetrical blocks, which in general have rectangular dimensions representing interactions in terms of volume–(discontinuous)surface and (boundary)surface–volume integration. In case of homogeneous scatterers, the last hybrid cluster trees are just a transpose of each other but in general they are not.

3.3 Rank function

As shown in (10), given a prescribed accuracy, the number of interpolation points p increases with electric size for electrodynamic problems. Such an increase is modeled in

$$\|g(\boldsymbol{r},\ \boldsymbol{r}') - \tilde{g}(\boldsymbol{r},\ \boldsymbol{r}')\|_{\infty,\,\Omega_t\times\Omega_s} \le \frac{4ed}{\pi}\left(\alpha_p\right)^{2d} p \frac{1}{\mathrm{dist}\left(\Omega_t,\ \Omega_s\right)} \times \left[1 + \sqrt{2}\eta\left\{k_0\ \mathrm{dist}\left(\Omega_t,\ \Omega_s\right) + 1\right\}\right] \times \left[1 + \frac{2}{\sqrt{2}\eta\left\{k_0\ \mathrm{dist}\left(\Omega_t,\ \Omega_s\right) + 1\right\}}\right]^{-p} \tag{10}$$

doi: 10.1049/iet-map.2013.0090

[7] by a rank function given by

$$k_{\text{var}}(t) = p^3(t) = \left[\hat{a} + \hat{b}\left(L - l(t)\right)\right]^3 \tag{11}$$

where $\hat{a}$ and $\hat{b}$ are constant coefficients, $l(t)$ denotes the tree level of cluster t with level zero being the root level of the inverted tree and L is the maximum tree level which has admissible blocks. In this section, we provide a detailed analysis of the rank function and discuss the choice of the two constant coefficients $\hat{a}$ and $\hat{b}$ for achieving a prescribed accuracy.

It is evident that in the above rank function, the number of interpolation points p is defined as a function that linearly increases with tree level L–l. For small and medium electric sizes, the growth rate of p with respect to electric size and hence tree level, required by accuracy of the interpolation based $\mathcal{H}^2$-representation, is not that fast yet. In other words, it has not reached its asymptotic growth rate suggested by (10). As a result, the p determined by accuracy can be closely bounded by the p determined by rank function. To give an example, in Fig. 1, we plot p determined by rank function with $\hat{a} = 5$ and $\hat{b} = 2$ with respect to L–l in comparison with p determined by accuracy of the interpolation based $\mathcal{H}^2$-representation for three different electric sizes from 3λ to 26λ of a perfect electric conductor sphere example. The accuracy of the interpolation-based $\mathcal{H}^2$-representation ε_{inp}, which is chosen as 0.01, is defined as $\|\boldsymbol{G} - \tilde{\boldsymbol{G}}\|_F / \|\boldsymbol{G}\|_F$ for each admissible block with $\tilde{\boldsymbol{G}}$ being the $\mathcal{H}^2$-representation of $\boldsymbol{G}$. It should be noted that not only the three electric sizes, but also a range of electric sizes are involved in this example since for each of the three electric size cases, each tree level also corresponds to a different electric size which increases from L–$l = 0$ to the largest L–l in the given case. It is evident from Fig. 1 that in the entire range of electric sizes being investigated, the p determined by accuracy of the interpolation-based $\mathcal{H}^2$-representation is well bounded by that determined by rank function with a suitable choice of $\hat{a}$ and $\hat{b}$, and also closely.

Theoretically speaking, the rank function can be used to model the rank's growth with electric size in any finite range of electric sizes. However, since the interpolation-based $\mathcal{H}^2$-representation is not efficient for solving electrically large problems as the resultant rank is too large, we only use the interpolation-based $\mathcal{H}^2$-representation for electrically small or medium-sized problems. Therefore the rank function is also used in the range from small to medium electric sizes. In this range, with the use of rank function, not only the accuracy of the interpolation-based $\mathcal{H}^2$-representation is well controlled, but also both storage and matrix–vector multiplication cost can be made to linearly scale with unknown number N, whose details are given in Section 4.

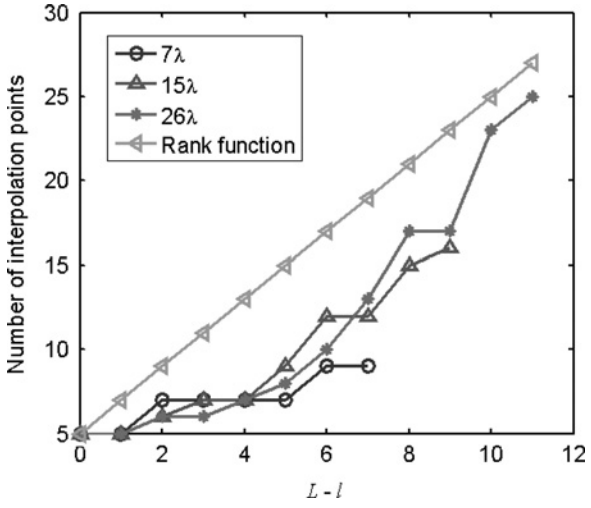

Fig. 1 *Comparison between the number of interpolation points p determined by the rank function and that determined by accuracy of the interpolation-based approximation*

The choice of constant coefficients $\hat{a}$ and $\hat{b}$ can be readily understood from Fig. 1. The $\hat{a}$ is nothing but the number of interpolation points p at level $(L$–$l) = 0$, that is, $l = L$. At this level, we can choose $\hat{a}$ to ensure that the accuracy of the interpolation-based $\mathcal{H}^2$-representation satisfies the prescribed accuracy ε_{inp}. This can be done by progressively increasing $\hat{a}$ until $\|\boldsymbol{G} - \tilde{\boldsymbol{G}}\|_F / \|\boldsymbol{G}\|_F \le \varepsilon_{\text{inp}}$ is satisfied for the largest admissible block at this level. Using the same approach, we can determine the number of interpolation points p required to achieve the prescribed accuracy at the largest L–l level for the given electric size range, from which and $\hat{a}$, slope $\hat{b}$ can be determined.

4 Fast $\mathcal{H}^2$-matrix-based VIE solver

The nested property of $\mathcal{H}^2$-matrices enables us to significantly reduce the complexity of VIE solvers. Before deriving the complexity, we introduce the following concepts and notations:

1. For each cluster $t \in T_{\mathcal{I}}$, the cardinality of the sets $\text{col}(t) := \{s \in T_{\mathcal{J}} : (t, s) \in T_{\mathcal{I}\times\mathcal{J}}\}$ and $\text{row}(t) := \{t \in T_{\mathcal{I}} : (t, s) \in T_{\mathcal{I}\times\mathcal{J}}\}$ is bounded by a constant C_{sp} [10].
2. Each non-leaf cluster t has two children, that is, $\#\text{children}(t) = 2$.

Owing to the nested property of an $\mathcal{H}^2$-matrix, we bypass the need of storing $\left(\boldsymbol{V}^t_{t\in T_{\mathcal{I}}}\right)$ for each cluster t. We only need to store $\left(\boldsymbol{V}^t_{t\in T_{\mathcal{I}}}\right)$ for leaf clusters, whereas for non-leaf clusters we store corresponding transfer matrices, which significantly reduce the total storage requirement. As a result, $\left(\boldsymbol{V}^t_{t\in T_{\mathcal{I}}}\right)$ can be stored as follows.

For each 'leaf' cluster $t \in \mathcal{L}_{\mathcal{I}}$, we have

$$\begin{aligned}&\text{Storage}\left(\boldsymbol{V}^t \text{ for all leaf clusters}\right)\\ &= \sum_{t\in\mathcal{L}_{\mathcal{I}}} O\left(k_{\text{var}}(t)\right)\#t \le O\left(\hat{a}^d\right)N\end{aligned} \tag{12}$$

For each 'non-leaf' cluster $t \in \mathcal{T}_{\mathcal{I}}$, we store the transfer matrices $\boldsymbol{E}^{t'}$ for all $t' \in$ children(t), which requires $O(k_{\text{var}}(t)\, k_{\text{var}}(t'))$ storage units, from which we obtain [7]

$$\begin{aligned}&\text{Storage}\left(\boldsymbol{V}^t \text{ for all non} - \text{leaf clusters}\right)\\ &= 8O\left[\left(\frac{2d(\hat{a}+\hat{b})}{\ln 1.5}\right)^{2d}\right]N\end{aligned} \tag{13}$$

For an admissible block b, we store the coupling matrix $\boldsymbol{S}^b$,

which requires $O(k_{\text{var}}^2(b))$ units of storage, thus

$$\text{Storage(all admissible blocks)} = \sum_{(t,s)\in\mathcal{L}^+_{\mathcal{I}\times\mathcal{J}}} O(k_{\text{var}}^2(b)) \le 4C_{sp}O\left[\left(\frac{2d(\hat{a}+\hat{b})}{\ln 1.5}\right)^{2d}\right]N \tag{14}$$

For an inadmissible block b, the admissibility condition implies that t and s have to be leaves of $T_{\mathcal{I}}$. Hence

$$\text{Storage(all inadmissible blocks)} \le \sum_{(t,s)\in\mathcal{L}^-_{\mathcal{I}\times\mathcal{J}}} O(n_{\min})^2 \le 2C_{sp}O(n_{\min}^2)N \tag{15}$$

Summing over (12)–(15), since C_{sp}, $n_{\min}$, $\hat{a}$, $\hat{b}$ and $d=3$ are constants, each of the $\boldsymbol{G}_i$ contributions and hence overall, $\boldsymbol{G}$ can be represented in $O(N)$ parameters and stored in $O(N)$ units, with the accuracy controlled to the same order by the rank function over a range of electric sizes.

Multiplying $\boldsymbol{G}_i$ with a vector $\boldsymbol{x}$ comprises of multiplying its 'inadmissible blocks' and 'admissible blocks' as represented in (8) with $\boldsymbol{x}$. For admissible blocks, we perform a tree traversal procedure consisting of forward transformation, coupling-matrix multiplication and backward transformation [7, 9, 10]. For inadmissible blocks, we perform a direct multiplication. As analysed in [7], the matrix–vector multiplication requires only $O(N)$ operations, with the accuracy controlled to the same order by the rank function for a range of N, and hence electric sizes.

The accelerated matrix–vector multiplication of the $\mathcal{H}^2$-representation of the dense part of VIE system [$\boldsymbol{G}$ of (2)] is put into use to solve the system itself using conjugate gradient method and bi-conjugate gradient stabilised (BiCGStab) Method. Since each iteration involves a sparse matrix–vector multiplication associated with $\boldsymbol{\Lambda}$ and an efficient $\mathcal{H}^2$-matrix–vector multiplication for dense system $\boldsymbol{G}$, the proposed VIE solver generates error-controlled results in fast CPU time with significantly reduced memory consumption.

5 Numerical results

In order to demonstrate the accuracy and efficiency of the proposed $\mathcal{H}^2$-matrix-based VIE solver, we simulated a dielectric sphere, a homogeneous dielectric triangular rod and an inhomogeneous dielectric triangular rod.

5.1 Dielectric sphere

The accuracy of the proposed solver is tested on a dielectric sphere of radius a with $k_0a=0.408$ and $\varepsilon_r=36.0$ same as in [14]. The E-field result shows very good agreement with the reference result given in [14] as shown in Fig. 2*a*. In Fig. 2*b*, we plot the RCS computed from the proposed method. Excellent agreement with Mie Series solution can be observed. The $\mathcal{H}^2$-representation is achieved by using geometric splitting in the construction of the cluster trees. The admissibility parameter η is chosen to be 3.0. In the volume cases, $n_{\min}=80$ whereas $\hat{a}$ and $\hat{b}$ of the rank function in (11) are 2 and 0.334, respectively. For the surface cases, $n_{\min}=40$ whereas $\hat{a}$ and $\hat{b}$ of the rank function are opted to be 2 and 0.5, respectively.

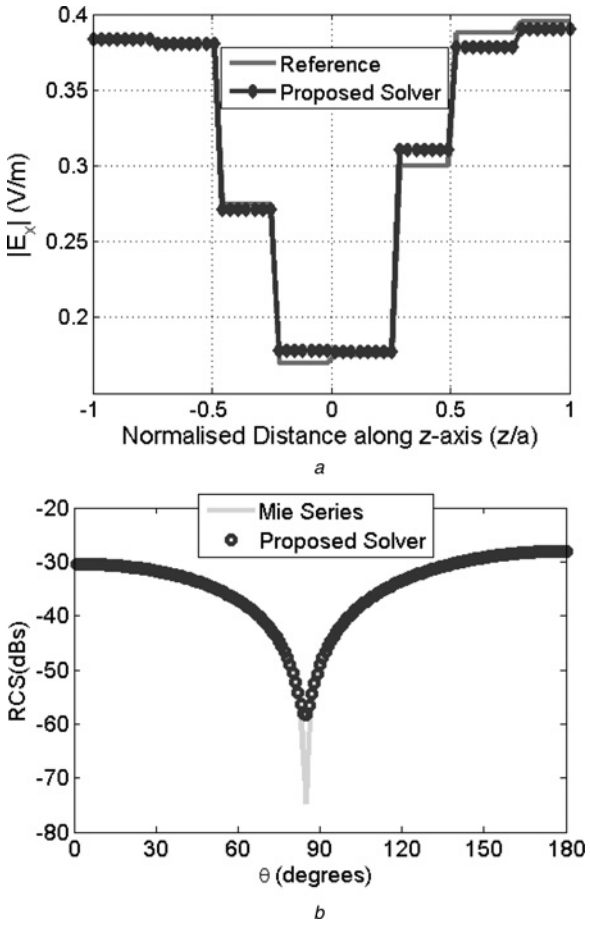

Fig. 2 *Simulation of a dielectric sphere ($\varepsilon_r=36.0$, $k_0a=0.408$)*
a Field along *z*-axis
b RCS

In order to demonstrate the efficiency of the proposed solver, the electric size of a dielectric sphere of $\varepsilon_r=4.0$ and radius 0.065 m is then allowed to increase by doubling the frequency from 300 MHz to 2.4 GHz, resulting in 1640–84856 unknowns ($\lambda/10$ meshing criterion). Fig. 3 depicts the relative error of the maximum admissible block for all the volume–volume, volume–surface and surface–surface components of matrix $\boldsymbol{G}$, as the electric size of the

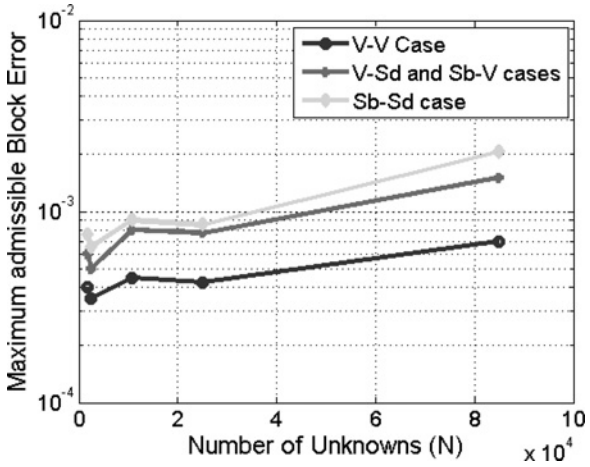

Fig. 3 *Upper bound on the $\mathcal{H}^2$-representation error for a dielectric sphere example*

doi: 10.1049/iet-map.2013.0090

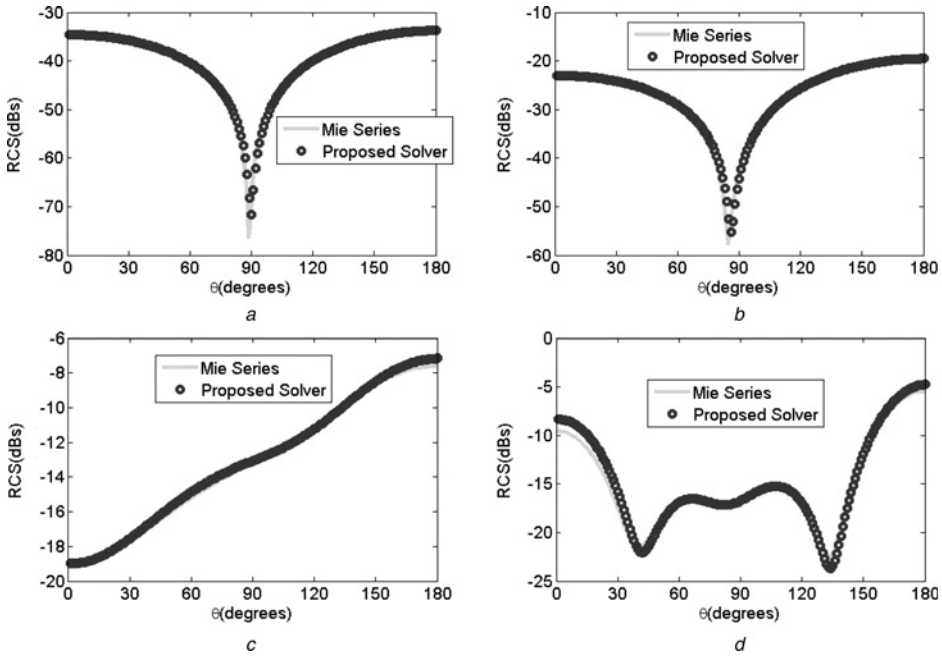

Fig. 4 *RCS comparison of a dielectric sphere*
a $k_0a = 0.408$
b $k_0a = 0.816$
c $k_0a = 1.632$
d $k_0a = 3.264$

sphere varies. A 10^{-3} order of accuracy is observed in the entire unknown range. The relative error of the maximal admissible block is computed as $\|\boldsymbol{G}^{(t,s)} - \tilde{\boldsymbol{G}}^{(t,s)}\| / \max\left(\|\boldsymbol{G}^{(t,t)}\|, \|\boldsymbol{G}^{(s,s)}\|\right)$. The corresponding RCS for all the electric sizes are compared against the analytical Mie Series solution and plotted in Fig. 4 from $k_0a = 0.408$ to $k_0a = 3.264$. Very good agreement can be observed. Note that the accuracy can be controlled to a user desired order by the choice of $\hat{a}$ and $\hat{b}$. If an accuracy better than that shown in Fig. 4 is pursued, one can increase $\hat{a}$ and $\hat{b}$ based on the scheme given in Section 3.3 until the desired accuracy is achieved. The ability of the proposed solver in correctly modelling and predicting the sharp whispering-gallery modes within the above resonance range is then tested against the Mie series solution. As shown in Fig. 5, the normalised backscatter RCS ($Q_b = \sigma_b/(\pi a^2)$, where σ_b is the back scattering radar cross section of the dielectric sphere) obtained by the proposed solver shows very good agreement with the Mie series solution throughout the frequency band. The sharp resonance frequency in the vicinity of electric size $k_0a = 2.7$ is well captured.

5.2 Homogeneous dielectric rod

In order to further elaborate the performance of the proposed solver, a dielectric triangular rod of $\varepsilon_r = 2.54$ as simulated in [14] is then simulated. As explained in [14], the RCS is computed for a triangular rod having the same cross-sectional area as that of a circular rod of radius 0.16 cm. In Fig. 6, we plot the RCS computed by the proposed

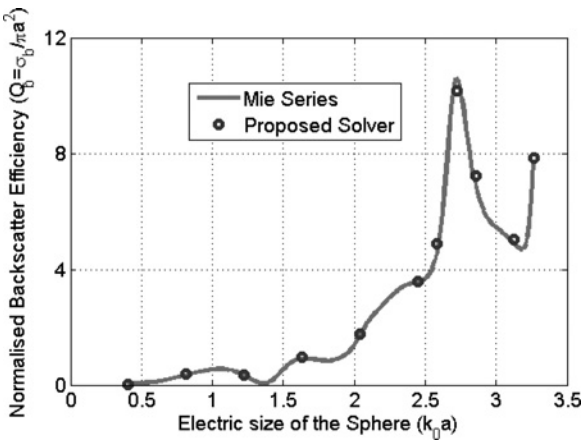

Fig. 5 *Normalised backscatter RCS (Q_b) of dielectric sphere as a function of electric size (k_0a)*

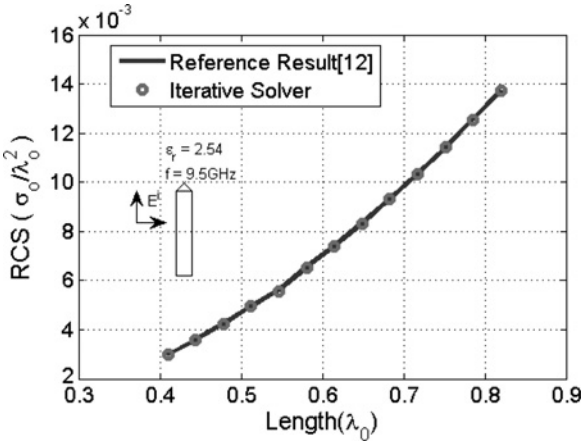

Fig. 6 *RCS of a triangular dielectric rod ($\varepsilon_r = 2.54$) of different lengths*

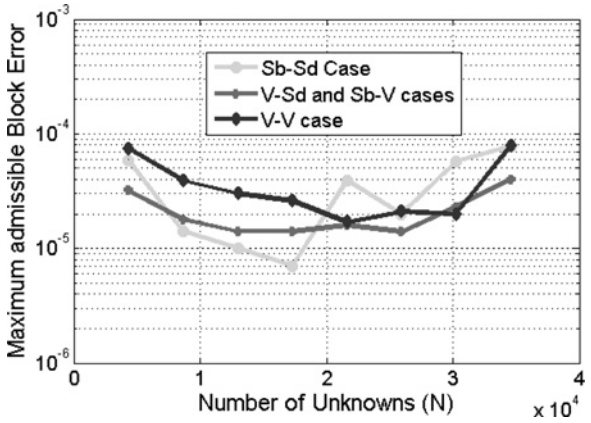

Fig. 7 *Upper bound on the $\mathcal{H}^2$-representation error for a dielectric rod example*

$\mathcal{H}^2$-based solver in comparison with that computed in [14]. Excellent agreement is observed. The time and memory efficiency of the proposed method is examined by increasing each cross-sectional side of the rod to 0.408λ and the length from 4λ to 32λ, resulting in 4336–34 576 unknowns with λ/10 being the meshing criterion. The admissibility parameter η is chosen as 0.95, and the 'leafsize' $n_{\min}$ is 80. Although for the x- and y-directions three interpolation points are chosen, for z-direction, $\hat{a}$ and $\hat{b}$ of the rank function are taken to be 4 and 4, respectively, for the volume-type cluster tree whereas for the surface-type both are selected to be 5 each. In Fig. 7, we plot the relative error of the maximal admissible block for all the volume–volume interaction, volume–surface interaction and surface–surface interaction blocks in matrix $\boldsymbol{G}$. A constant order of accuracy is observed in the entire electric size range. In Fig. 8*a*, we compare the memory requirement of the proposed method with that of a conventional solver. In Fig. 8*b*, we plot the solution time of the proposed solver in comparison with that of the conventional solver. The proposed solver demonstrates a clear linear scaling in the electric size range being investigated.

To demonstrate the capability of the proposed method in simulating electrically larger examples, an 80λ (86 416 unknowns) rod is simulated. To achieve 10^{-4} order of accuracy, $\hat{b}$ of the rank function is increased to 7 and 8, respectively, for volume and surface cluster trees. It costs the proposed solver only 13 Gb of memory as compared with 112 Gb cost by the conventional solver, and 3575.5 s for the solution as compared with 61 096 s cost by the

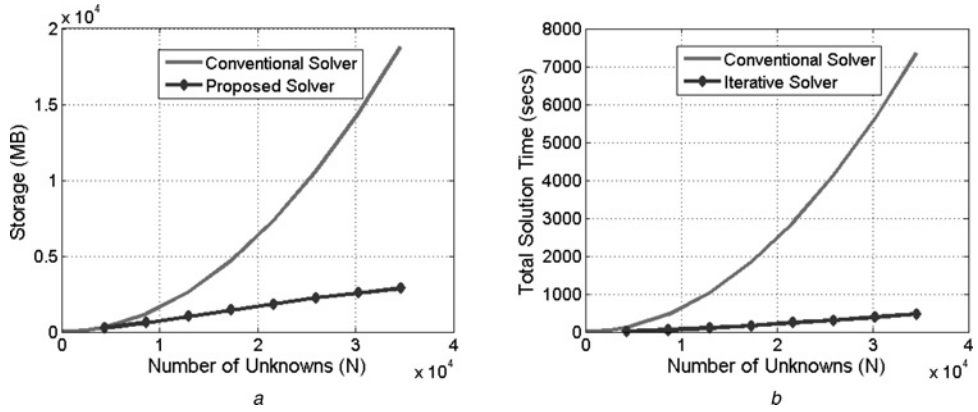

Fig. 8 *Performance comparison*

a Storage
b Solution time

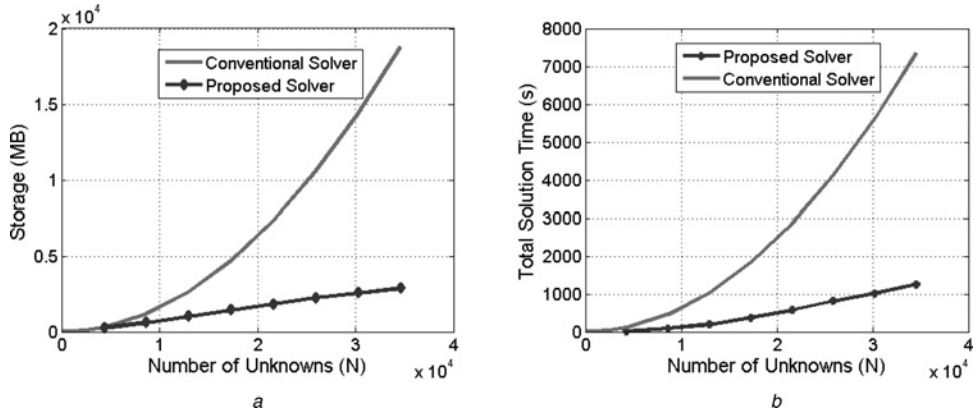

Fig. 9 *Performance comparison for an inhomogeneous rod example*

a Storage
b Solution time

doi: 10.1049/iet-map.2013.0090

conventional solver. The costs of the conventional solver are extrapolated based on its square complexity.

5.3 Inhomogeneous dielectric rod

An inhomogeneous triangular dielectric rod of cross-sectional dimensions of 0.408λ with half of the rod being of $\varepsilon_r = 2.54$ and the other half of $\varepsilon_r = 4.0$ is then simulated. All the parameters are kept the same as in the homogeneous case simulated in the previous example, which results in the same order and trend of accuracy and memory requirements as in the previous example. The comparison of memory resources used and the solution times for the conventional and proposed solver are shown in Fig. 9. Again, a significant reduction in CPU time and memory is observed. The cost of the proposed solver is higher than that shown in the previous example because the iteration number increases in this inhomogeneous example.

6 Conclusions

The $\mathcal{H}^2$-matrix-based representation of dense systems of equations is developed for a more general case of 3D volume integral equation which comprises of all possible forms of integrals. With such a representation, both memory consumption and time complexity of a matrix–vector multiplication are significantly reduced compared with the conventional VIE solvers. Numerical examples of homogeneous and inhomogeneous scatterers from small to tens of wavelengths have demonstrated the performance of the proposed $\mathcal{H}^2$-based VIE solver. The $\mathcal{H}^2$-representation of the VIE system is generated by an interpolation-based method with accuracy controlled by a rank function. In the future, we will explore other more efficient $\mathcal{H}^2$-representations of the VIE dense system so that even larger electric sizes can be efficiently handled on a single computer.

7 References

1 Chew, W.C., Jin, J.M., Michielssen, E., Song, J.M.: 'Fast and efficient algorithms in computational electromagnetics' (Artech House, Norwood, MA, 2001)

2 Bojarski, N.N.: '*k*-space formulation of the electromagnetic scattering problem'. Technical Report, AFAL-TR-71-75, Air Force Avionics Laborotory, 1971

3 Bleszynski, E., Bleszynski, M., Jarozewicz, T.: 'AIM: adaptive integral method for solving large-scale electromagnetic scattering and radiation problems', *Radio Sci.*, 1996, **31**, pp. 1225–1251

4 Ling, F., Okhamtovski, V.I., Harris, W., McCracken, S., Dengi, A.: 'Large-scale broad-band parasitic extraction for fast layout verification of 3D RF and mixed-signal on-chip structures', *IEEE Trans. Microw. Theory Tech.*, 2005, **53**, (1), pp. 264–273

5 Yilmaz, A.E., Jin, J.M., Michielssen, E.: 'A parallel FFT-accelerated transient field-circuit simulator', *IEEE Trans. Microw. Theory Tech.*, 2005, **53**, (9), pp. 2851–2865

6 Kapur, S., Long, D.E.: '*IES*^{3}: a fast integral equation solver for efficient 3-dimensional extraction'. IEEE/ACM Int. Conf. on Comput.-Aided Design Dig., November 1997, pp. 448–455

7 Chai, W., Jiao, D.: 'An $\mathcal{H}^2$-matrix-based fast integral-equation solver of reduced complexity and controlled accuracy for solving electrodynamic problems', *IEEE Trans. Antennas Propag.*, 2009, **57**, (10), pp. 3147–3159

8 Chai, W., Jiao, D.: '$\mathcal{H}$ - and $\mathcal{H}^2$ -matrix-based fast integral-equation solvers for large scale electromagnetic analysis', *IET Microw. Antennas Propag.*, 2010, **4**, (10), pp. 1583–1596

9 Borm, S.: '$\mathcal{H}^2$ -matrix approximation of integral operators by interpolation', *Appl. Numer. Math.*, 2002, **43**, pp. 129–143

10 Borm, S., Grasedyck, L., Hackbusch, W.: 'Hierarchical matrices', Lecture Note 21 of the Max Plack Institute for Mathematics in the Sciences, 2003

11 Chai, W., Jiao, D.: 'A theoretical proof on the error-bounded low-rank representation of integral operators for large-scale 3-D electrodynamic analysis'. IEEE Int. Symp. on Antennas and Propagation, 2012

12 Chai, W., Jiao, D.: 'A comprehensive theoretical study on the rank of the integral operators for large-scale electrodynamic analysis'. TR-ECE-12-09, School of Electrical and Computer Engineering, Purdue University, 2012, URL: http://www.docs.lib.purdue.edu/ecetr/436

13 Chai, W., Jiao, D.: 'A complexity-reduced $\mathcal{H}$ -matrix based direct integral equation solver with prescribed accuracy for large-scale electrodynamic analysis'. IEEE Int. Symp. on Antennas and Propagation, July 2010

14 Schaubert, D.H., Wilton, D.R., Glisson, A.W.: 'A tetrahedral modeling method for electromagnetic scattering by arbitrarily shaped inhomogeneous dielectric bodies', *IEEE Trans. Antennas Propag.*, 1984, **32**, pp. 77–85